Stochastic thermodynamics of a confined colloidal suspension under shear flow

Sascha Gerloff[*] and Sabine H. L. Klapp[†]

Institut für Theoretische Physik, Hardenbergstraße 36, Technische Universität Berlin, D-10623 Berlin, Germany

Based on Brownian dynamics simulations, we investigate the thermodynamic signatures of nonequilibrium steady states in a confined colloidal suspension under shear flow. Specifically, we consider a thin film consisting of charged particles in narrow slit-pore confinement, forming two layers with quadratic in-plane structure in equilibrium. This many-body system displays three distinct steady states, characterized by unique dynamical and rheological response to the applied shear flow. Calculating the work and heat, we find that both quantities indicate the different states by their mean and by their distributions. A particularly interesting situation occurs at large shear rates, where the particles perform a collective zigzag motion. Here, we find a bistability regarding the degree of phase synchronization of the particle motion. It turns out that this bistability is key to understanding the resulting ensemble-averaged work distributions. For all states, we compare the work and heat distributions to those of effective single-particle systems. By this, we aim at identifying the many-body character of the stochastic thermodynamic quantities.

I. INTRODUCTION

In the past decades, the framework of stochastic thermodynamics (ST) [1–4] has attracted interest for a wide range of nonequilibrium systems, including molecular motors [5–7], thermal conductors [8], active matter [9–11], quantum systems [12–14], and colloidal systems [15–17]. One common feature of these systems is that they are subject to noise stemming from the coupling to a heat bath. As a consequence, energy changes in the form of heat and work as well as the entropy production become fluctuating quantities. These fluctuations can become especially important for small systems, such as molecular motors, which are largely driven by diffusion similar to a thermal ratchet [5]. One important insight from ST is that these fluctuations can be restricted by fluctuation theorems, representing a generalized, stochastic counterpart of the second law of thermodynamics [1,18–20].

In the present study we apply concepts of ST to a driven colloidal suspension. The goal is to explore the fluctuating thermodynamic quantities for nonequilibrium many-particle systems. Indeed, in the context of ST, colloidal systems have proven to be a powerful test bed in both theoretical [1] and experimental investigations [4]. Most of the research in this area has been concerned with single-particle systems, such as a single colloid driven by a modulated [21,22] or translated optical trap [15,18]. Further examples involve a colloidal particle driven over a periodic potential [23,24], suspended in an active bath [10,16] or under delayed feedback control [17], to name a few. In contrast, systems containing many interacting particles have been less explored, although one of the first reports of a fluctuation theorem was concerned with sheared molecular suspensions [25]. Only recently, concepts of ST have been applied to systems with interacting degrees of freedom [26], examples being coupled oscillators [27], driven colloidal monolayers [28], soft particulate media in shear flow [29], flow-driven polymer chains [30], and active matter [9]. A particularly interesting question for a many-particle system is how interaction-induced transitions between dynamical states are reflected in ST quantities and their respective distributions.

In this study, we investigate, based on Brownian dynamics (BD) simulations, a dense colloidal suspension confined to a narrow slit pore, which is driven by a linear shear flow. We use this system as a test bed to explore the thermodynamic behavior of an interacting, flowing system. Indeed, the interplay of narrow slit-pore confinement, particle interactions, and shear flow induces rich nonlinear dynamics, such as shear-induced melting and crystallization [31,32], buckling [20,33], as well as density heterogeneities [34]. Following previous studies by us [32,34,35], we focus on a system consisting of two layers with quadratic in-plane order in equilibrium, whose dynamical and structural response to the shear flow is characterized by three distinct steady states. We investigate the signatures of the steady states in two prominent (stochastic) thermodynamic quantities, that is, work and heat. To this end, we study the mean values and distribution functions as functions of shear rate and time. Analyzing the distributions provides, on the one hand, information on the occurrence of rare events such as extraction of heat from the bath. On the other hand, and this turns out to be particularly relevant for the present system, the distributions reveal information about the *coherence* of particle motion.

We also compare our numerical results with those of appropriate single-particle systems, which reveal many similarities particularly for small shear rates. In contrast, at large shear rates, the work in the steady state is characterized by a bistability with regard to the degree of phase synchronization of the particle motion. Here, the many-body nature of the system,

---

[*]s.gerloff@tu-berlin.de

[†]klapp@physik.tu-berlin.de

which is reflected in the bistability, has a severe impact on the resulting work fluctuations.

The paper is structured as follows. In Sec. II we briefly describe the model system and recapitulate the resulting dynamical behavior. Section III summarizes the concepts of stochastic thermodynamics of flowing systems [36], which we then apply to our sheared colloidal film in Sec. IV. In Sec. V we discuss, in particular, the bistability of the running state and its impact on the thermodynamics. Finally, we compare our results to an effective single-particle system in Sec. VI and conclude in Sec. VII.

II. PLANAR SLIT-PORE SYSTEM

A. Models and simulation details

Following previous studies [32,34,35], we consider a colloidal suspension of charged macroions on a coarse-grained level, where the macroions interact via a combined *Yukawa*-like and soft-sphere potential. The parameters are set in accordance with real suspensions of silica particles [37]. The slit-pore geometry is mimicked by two plane-parallel soft walls extended infinitely in the x and y directions and separated in the z direction by a distance L_z. The colloid-wall interaction is given by an integrated soft-sphere potential [38].

We perform (overdamped) BD simulations to examine the nonequilibrium properties and dynamics of our model system. To implement the flow we employ a linear shear term (for justification, see below), thereby following earlier simulation studies [39,40]. Specifically, the position $\mathbf{r}_i$ of particle i is advanced according to the equation of motion [32]

$$\dot{\mathbf{r}}_i(t) = \mu \, \mathbf{F}_i(\{\mathbf{r}\}) + \dot{\mathbf{W}}_i(t) + \dot{\gamma} z_i \mathbf{e}_x, \qquad (1)$$

where $\mathbf{F}_i$ is the total conservative force (stemming from two-particle and particle-wall interactions) acting on particle i and $\{\mathbf{r}\} = \mathbf{r}_1, \ldots, \mathbf{r}_N$ is the set of particle positions. Within the framework of BD, the influence of the solvent is mimicked by a single-particle frictional and random force. The mobility is given as $\mu = D_0 / k_B T$, where D_0 is the short-time diffusion coefficient, k_B is the Boltzmann constant, and T is the temperature. The random force is modeled by random Gaussian displacements $\delta \mathbf{W}_i$, with zero mean, variance $2 D_0 \delta t$ for each Cartesian component, and the discrete time step δt. The timescale of the system is set to $\tau = d^2 / D_0$, which defines the so-called Brownian time. The last term in Eq. (1), $\dot{\gamma} z_i \mathbf{e}_x$, represents a linear shear flow in the x direction and gradient in the z direction. The strength of the flow is characterized by the uniform shear rate $\dot{\gamma}$. This ansatz seems plausible for systems where the motion of the walls is not directly coupled to that of the colloids, an example being a system consisting of charged colloids and likewise charged walls, where the distance between the colloids and wall particles is naturally rather large. We note that despite the application of a linear shear profile, the real, steady-state velocity profile resulting from the simulations can be nonlinear [33,41].

The present simulation approach has also been employed in other recent simulation studies of sheared colloids [40,42,43]; the same holds for the fact that we neglect hydrodynamic interactions.
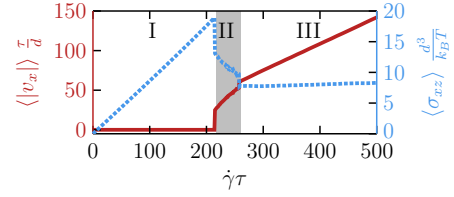

FIG. 1. Mean absolute velocity in x direction, $\langle |v_x| \rangle$ (solid red), and mean shear stress component, $\langle \sigma_{xz} \rangle$ (dashed blue), as a function of the dimensionless shear rate $\dot{\gamma} \tau$. The three distinct steady states are indicated by I (locked), II (disordered running), and III (ordered running). They correspond to a quadratic, disordered, and hexagonal translational structure, respectively.

B. Shear-induced transitions in a bilayer system

Here, we recapitulate the well-explored dynamical behavior of a system which, in equilibrium, consists of two layers of colloidal particles with quadratic crystalline in-plane order [32,35]. Starting from equilibrium and applying a linear shear flow, the system displays three distinct steady states, as reflected in Fig. 1 by the nonlinear average absolute velocity $\langle |v_x| \rangle$ and shear stress $\langle \sigma_{xz} \rangle$ as a function of the dimensionless shear rate $\dot{\gamma} \tau$. In the first (locked) steady state, the shear is insufficient to break the quadratic crystalline order, leading to elastic deformations while keeping the particles locked ($\langle |v_x| \rangle = 0$). Increasing the shear rate, the system undergoes a depinning transition to the second (disordered running) state at a critical shear rate $\dot{\gamma}_c \tau \approx 216$ [34], introducing net motion of the particles ($\langle |v_x| \rangle > 0$) and breaking the crystalline in-plane order. Another type of crystalline order is recovered for even larger shear rates ($\dot{\gamma} \tau \approx 260$), where the colloids reorganize into layers with hexagonal in-plane order, performing a collective zigzag motion which characterizes the third (ordered running) steady state. We note that the presence of a depinning transition, reflected by the sudden onset of nonzero average velocity, strongly reminds us of the behavior observed in colloidal monolayers driven over a periodic substrate [34]. However, there is one conceptual difference: In our system there is no externally fixed substrate; rather the particles in one layer feel a fluctuating potential stemming from the other layer.

In the present study, we investigate the consequences of the nontrivial dynamical behavior of the sheared film from the point of view of (stochastic) thermodynamics.

III. STOCHASTIC THERMODYNAMICS

Following Sekimoto's concept of stochastic energetics [2], the terms appearing in the first law of thermodynamics,

$$dU = \delta w - \delta q, \qquad (2)$$

can be expressed on the basis of individual fluctuating particle trajectories. Here, dU is the total change of internal energy, δw is the work applied to the system, and δq is the heat dissipated *into* the bath. Considering, for simplicity, a (one-dimensional) overdamped stochastic process described by the Langevin equation $\dot{x} = -\mu \, \nabla_x U(x, t) + \dot{W}$, the left-hand

side of Eq. (2) is given by

$$dU = \frac{\partial U}{\partial t} \circ dt - \frac{1}{\mu}[\dot{x} - \dot{W}] \circ dx, \qquad (3)$$

where, in the second term, we used that $\nabla_x U(x,t) = -\mu^{-1}[\dot{x} - \dot{W}]$, according to the Langevin equation. In Eq. (3), the symbol $\circ$ denotes the integration using the Stratonovich calculus. The first term of Eq. (3) contains the temporal variation of the potential energy due to an external control protocol; it corresponds to the work δw applied to the system. The second term only involves contributions from the solvent, i.e., the friction forces $\mu^{-1}\dot{x}$ as well as the random forces $\mu^{-1}\dot{W}$; it can be identified as the heat δq dissipated into the bath [1,2]. Note that both δw and δq are stochastic quantities with generally time-dependent distributions $P(w)$ and $P(q)$.

A. Extension to many-particle systems in flow

While the extension of ST to interacting many-body systems is straightforward, special care has to be taken when applying a flow field, as noted first in Ref. [36]. The complications arise from the fact that the expressions for the work and heat as introduced by Sekimoto are *not* frame-invariant. In particular, if the explicit time dependence of the potential energy vanishes in the comoving frame, the work δw vanishes. Therefore, the common expressions for the work and heat [see Eq. (3) below] are only valid in the frame of reference where the solvent is at rest.

To account for the flow correctly, the authors of Ref. [36] proposed generalized expressions for the work and heat rates, which are independent of the particular choice of the frame of reference. The key idea is to add an advection term to the work rate and to measure the displacement of particles with respect to the flow. The resulting work rate in a many-particle flowing system is given by

$$\dot{w}(t) = \sum_i \dot{w}_i(t) = \sum_i \left\{ \left. \frac{\partial U(\{\mathbf{r}\},t)}{\partial t} \right|_{\mathbf{r}_i} \right.$$
$$\left. - \mathbf{u}(\mathbf{r}_i,t) \cdot \mathbf{F}_i(\{\mathbf{r}\},t) + \mathbf{f}_i \cdot [\dot{\mathbf{r}}_i(t) - \mathbf{u}(\mathbf{r}_i,t)] \right\}, \quad (4)$$

where $\dot{w}_i(t)$ is the work rate corresponding to particle i. This expression takes into account three possible sources of work. The first term in Eq. (4) corresponds to the temporal variation of the potential energy $U(\{\mathbf{r}\},t)$ acting on particle i due to an external control protocol. The second term corresponds to the advection of particles due to an external flow with velocity $\mathbf{u}(\mathbf{r}_i,t)$ against the conservative forces $\mathbf{F}_i(\{\mathbf{r}\},t) = -\nabla_i U(\{\mathbf{r}\},t)$. The third term corresponds to the displacement of particles relative to the imposed external flow due to external (nonconservative) forces $\mathbf{f}_i$ acting on particle i.

The heat rate then follows from the first law of thermodynamics [see Eq. (2)] as

$$\dot{q}(t) = \dot{w}(t) - \frac{d U(\{\mathbf{r}\},t)}{dt} = \sum_i \dot{q}_i(t)$$
$$= \sum_i [\mathbf{f}_i + \mathbf{F}_i(\{\mathbf{r}\},t)] \cdot [\dot{\mathbf{r}}_i(t) - \mathbf{u}(\mathbf{r}_i,t)], \qquad (5)$$

where $d U/dt = \partial U/\partial t + \sum_i \dot{\mathbf{r}}_i(t) \cdot \nabla_i U$ denotes the total time derivative of the potential energy. Note that according to Eq. (5), the heat dissipated into the bath vanishes whenever the particles follow the external flow perfectly, i.e., $\dot{\mathbf{r}}_i(t) = \mathbf{u}(\mathbf{r}_i,t)$. Integrating the work and heat rates over time, we obtain the work and heat

$$w(t) = \sum_i w_i(t) = \sum_i \int_0^t \dot{w}_i(t')dt' \qquad (6)$$

and

$$q(t) = \sum_i q_i(t) = \sum_i \int_0^t \dot{q}_i(t')dt', \qquad (7)$$

respectively. Here, the expressions in Eqs. (4)–(7) were derived using the Stratonovich calculus. Therefore, all derivates and integrals need to be performed using the midpoint rule, according to the Stratonovich interpretation (for more details see Appendix A).

B. Application to the sheared colloidal film under external flow

We now apply the expressions for the work and heat rates to the sheared colloidal film. To this end, we interpret the shear term in Eq. (1) as an external flow, i.e., $\mathbf{u}_i = \dot{\gamma} z_i \mathbf{e}_x$. Further, the external force $\mathbf{f}_i = 0$ is set to zero, since the system is solely driven by the shear flow. Finally, we note that the total potential energy is not explicitly time-dependent. The general expressions (4) and (5) then simplify to

$$\dot{w}(t) = -\sum_i \mathbf{u}(\mathbf{r}_i) \cdot \mathbf{F}_i(\{\mathbf{r}\}) \qquad (8)$$

and

$$\dot{q}(t) = \sum_i \mathbf{F}_i(\{\mathbf{r}\}) \cdot [\dot{\mathbf{r}}_i(t) - \mathbf{u}(\mathbf{r}_i)] \qquad (9)$$

for the work and the heat rate, respectively.

Inspecting Eq. (8), we find that the work rate is closely related to the instantaneous shear stress, which defines the mechanical response of the system to the applied shear. This follows immediately if we insert the linear shear flow $\mathbf{u}_i = \dot{\gamma} z_i \mathbf{e}_x$ into Eq. (8), yielding

$$\dot{w}(t) = -\dot{\gamma} \sum_i z_i F_{x,i}(\{\mathbf{r}\}) = \dot{\gamma} \sigma_{xz} V, \qquad (10)$$

where σ_{xz} is the x-z component of the virial stress tensor $\boldsymbol{\sigma} = -V^{-1} \sum_i \mathbf{r}_i \mathbf{F}_i$, and V is the volume of the slit pore. This relation was also reported in other studies concerning shear-driven systems [29,44]. Further, a similar relation was stated in an early study by Evans *et al.* [25], which proposes a linear relation between the heat used to thermostat the molecular dynamics simulations, and the shear stress.

From Eqs. (8) and (9), the time-dependent work and heat are obtained by numerical integration (see Appendix A) using Eqs. (6) and (7).

An alternative interpretation of the shear term in the equation of motion [see last term in Eq. (1)] is presented in Appendix B, where we interpret the shear as an external force. This situation resembles that discussed in a recent experimental study of colloidal monolayers driven over a periodic laser field [28].
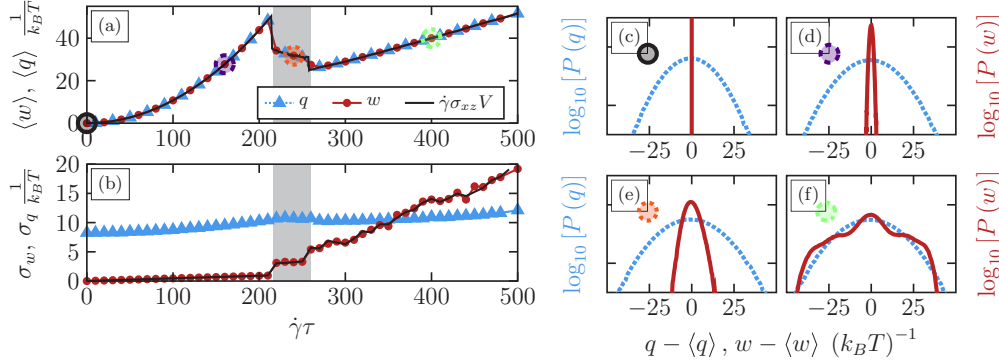
FIG. 2. (a) Mean value and (b) standard deviation of the work (red circles) and heat (blue triangles) related to the sheared colloidal film integrated over short time intervals ($\Delta t = 10^{-5}\tau_B$); see Eq. (8) and Eq. (9), respectively. The mean is calculated by averaging over times τ_B and 100 *independent* systems. The black solid line stems from the exact relation given in Eq. (10). (c)–(f) Corresponding distributions of the work (solid, red) and heat (dashed, blue) for exemplary shear rates $\dot{\gamma}\tau = 0, 160, 240, 400$, respectively. These shear rates are marked in (a) with black, purple, orange, and green circles and correspond to the equilibrium, locked (I), disordered running (II), and ordered running (III) state.

IV. NUMERICAL RESULTS

A. Mean work and heat

To start with, we investigate the mean work $\langle w \rangle$ and heat $\langle q \rangle$ as a function of the shear rate, one main question being whether these quantities reflect the shear-induced transitions described in Sec. II B. To this end we integrate the work w and heat q (before averaging) over short time intervals $\Delta t = 10^{-5}\tau_B$. In this limit, w and q are determined by the corresponding rates, e.g., $w \approx \dot{w}\Delta t$ and $q \approx \dot{q}\Delta t$. The mean $\langle \cdot \rangle$ is computed by analyzing trajectories for 100 *independent* systems at random times, yielding a combined ensemble and time average. The results are shown in Fig. 2(a).

We first investigate the work. In equilibrium ($\dot{\gamma}\tau = 0$), we find that $\langle w \rangle = 0$, as expected since no work is performed on the system. Applying a shear flow, $\langle w \rangle$ displays a pronounced increase, reflecting that more and more work is consumed to maintain the quadratic crystalline structure characterizing the locked (I) steady state ($\dot{\gamma}\tau < 216$). Increasing the shear beyond the depinning threshold ($\dot{\gamma}\tau > 216$), $\langle w \rangle$ jumps to smaller values and continues to decrease with the shear rate, corresponding to the disordered running (II) state, which appears upon breaking the quadratic crystalline order. For shear rates $\dot{\gamma}\tau > 260$, $\langle w \rangle$ performs another jump to smaller values and a subsequent increase, corresponding to the re-arrangement of the colloids in hexagonal layers moving in a collective zigzag motion [ordered running (III) state]. The overall behavior of $\langle w \rangle$ is thus fully determined by that of $\langle \sigma_{xz} \rangle$ [35], as expected from Eq. (10).

The mean heat (dissipated into the bath) displays the same behavior, not only from a qualitative point of view but also quantitatively. Indeed, we find that $\langle w \rangle = \langle q \rangle$ for all considered shear rates, including the disordered running (II) state. Such an equality of *averaged* work and dissipated heat is expected in steady states, where the total time derivative of the energy should vanish on average. While this is intuitively clear in the locked (I) and ordered running (III) states, the disordered running state (II) is more subtle: Here, the negative slope of the shear stress suggests that this state is mechanically unstable and thus *not* a true steady state for finite times. In

fact, state (II) is characterized by extremely long relaxation times [35]. Therefore, we think that there is indeed a very small difference between $\langle w \rangle$ and $\langle q \rangle$ in the disordered running (II) state. This difference reflects the very slow relaxation dynamics, but it is too small to be detected in our simulations. That is, on the timescales considered, the disordered running (II) state *acts* like a steady state ($\langle w \rangle \approx \langle q \rangle$), while in reality it might be a transient state after all. To confirm this point, further studies are necessary.

Overall, we find that the transitions between the different steady states (I–III) are clearly reflected in both the mean work $\langle w \rangle$ and heat $\langle q \rangle$. The corresponding shear rate dependence is closely related to that of the shear stress, as seen in Eq. (10).

Finally, in Fig. 3, we have plotted the mean work and heat as a function of the integration time t for four shear rates $\dot{\gamma}\tau = 0, 160, 240, 400$ corresponding to the different steady states. In equilibrium ($\dot{\gamma}\tau = 0$), both the mean heat and work remain zero for all times, due to the absence of any driving forces. Applying the linear shear flow, we observe a linear increase in time of the mean heat and work for all shear rates. That is, the mean heat and work *rates* are constant, and *on average* their shear rate dependency is given by the short-time heat and work; see Fig. 2(a). We note already here that we can understand the linear time dependence as well as the quadratic increase of the mean work and heat in the locked (I) state by comparing to a well-studied single-particle system consisting of an overdamped colloidal particle trapped in a harmonic potential, as discussed in Sec. IV C.
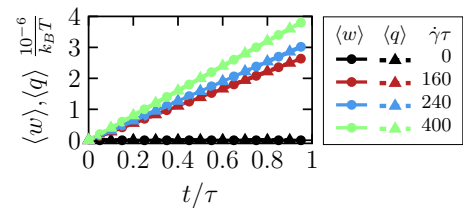

FIG. 3. Mean work $\langle w \rangle$ and heat $\langle q \rangle$ over integration time t for four different shear rates $\dot{\gamma}\tau = 0, 160, 240, 400$ (black, red, blue, green).

B. Work and heat distribution

While the work and heat are the same *on average* $\langle w \rangle = \langle q \rangle$ for all steady states, this does not hold for the individual realizations of w and q, which are subject to fluctuations. To investigate these fluctuations, we consider the work and heat distributions, $P(w)$ and $P(q)$. Results are plotted in Figs. 2(c)–2(f) for four exemplary shear rates $\dot{\gamma}\tau = 0, 160, 240, 400$, corresponding to equilibrium and the three steady states, respectively. These results refer to a fixed, small integration time $t = 10^{-5}\tau_B$.

Focusing first on $P(w)$ and starting in equilibrium [$\dot{\gamma}\tau = 0$; see Fig. 2(c)], we find that $P(w)$ is delta-peaked. This directly follows from Eq. (10), which shows that the work rate vanishes if no shear is applied to the system. Applying a finite shear flow, the work turns out to be Gaussian distributed for all shear rates corresponding to the locked (I) state [$\dot{\gamma}\tau < 216$; see Fig. 2(d)]. That is, the skewness of the distribution

$$\gamma_1^w = \frac{\langle (w - \langle w \rangle)^3 \rangle}{\sigma_w^3} \tag{11}$$

vanishes and the kurtosis fulfills

$$\gamma_2^w = \frac{\langle (w - \langle w \rangle)^4 \rangle}{\sigma_w^4} \approx 3, \tag{12}$$

where

$$\sigma_w = \sqrt{\langle (w - \langle w \rangle)^2 \rangle} \tag{13}$$

is the standard deviation. Once the system melts [$\dot{\gamma}\tau > 216$; see Fig. 2(e)], $P(w)$ becomes slightly skewed in positive direction with $\gamma_1^w \approx 0.225$. Finally, for large shear rates [$\dot{\gamma}\tau > 260$; see Fig. 2(f)], $P(w)$ displays pronounced asymmetric shoulders on both sides. These stem from the collective hopping of the colloidal layers, which characterize the order running (III) state. In fact, we find that the particular shape of $P(w)$ is a result of a bistability, which we discuss in more detail in Sec. V.

For the heat distribution $P(q)$, we find that, already in equilibrium, $P(q)$ is Gaussian distributed, with vanishing skewness ($\gamma_1^q = 0$) and kurtosis $\gamma_2^q = 3$. This remains true for all steady states. In particular, we do not observe any shoulders in $P(q)$ for the ordered running (III) state, contrary to the work distribution $P(w)$.

We now turn to the dependence of the distribution on the integration time t. In equilibrium, the work distribution remain delta-peaked for all times, whereas the heat distribution quickly converges towards a static Gaussian distribution, as expected from the central limit theorem. Applying a finite shear flow with $\dot{\gamma}\tau < 216$ [locked (I) state], the work and heat distributions collapse over time to one Gaussian distribution, shown in Fig. 4(b) for $\dot{\gamma}\tau = 160$. While the mean of this distribution increases linearly in time, the standard deviation $\sigma_{w/q}$ increases approximately with $\sqrt{2 k_B T \langle w \rangle} \propto \sqrt{t}$, plotted in Fig. 4(a). This behavior is reminiscent of that found for particles trapped in harmonic traps, as we will discuss in more detail in Sec. IV C.

In the disordered running (II) state, the work and heat distributions again collapse onto a single distribution over
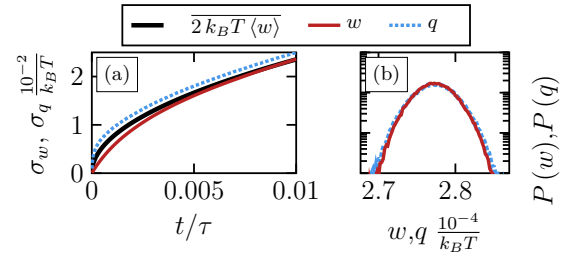

FIG. 4. (a) Standard deviation of the heat (dashed, blue) and work distribution (solid, red) as a function of time for the locked (I) state $\dot{\gamma}\tau = 160$. The square root of the mean value is plotted as a reference. (b) Corresponding distributions for integration times $t = 0.01\tau$.

time, as shown in Fig. 5(c) for $\dot{\gamma}\tau = 240$. For long integration times, the resulting distributions become strongly asymmetric, with the skewness saturating at $\gamma_1^{w/q} = 0.625$; see Fig. 5(b). In contrast to the locked (I) state, however, $\sigma_{w/q}$ now increases approximately linear with the mean $\propto \langle w \rangle$, shown in Fig. 5(a).

Finally, in the ordered running (III) state, work and heat distributions display complex cyclic evolution, which we will discuss in Sec. V B.

C. Comparison to a single particle in a harmonic trap (SP1)

In equilibrium ($\dot{\gamma} = 0$), the particles are locked to a quadratic crystalline structure, where the position of each particle fluctuates around its lattice side. For small fluctuations, we can approximate the potential energy experienced by one particle by a harmonic potential centered around its equilibrium position. The work $P(w)$ and heat distribution $P(q)$ for a single particle trapped in a harmonic trap $U(x) = (k/2)x^2$ can be calculated analytically [45]: In equilibrium $P(w)$ is given by a delta distribution at zero, while $P(q)$ takes the form of a zeroth-order Bessel function of second type. For the colloidal film considered here, we also find a delta distribution for $P(w)$ but the many-body heat distribution is Gaussian. This is a result of the central limit theorem, which states that the distribution of the sum $q = \sum_{i=1}^{N} q_i$ of *independent* and *identically distributed* random variables q_i will always converge towards a Gaussian distribution for large numbers $N \to \infty$ of summands. Here, q_i is the heat per particle.
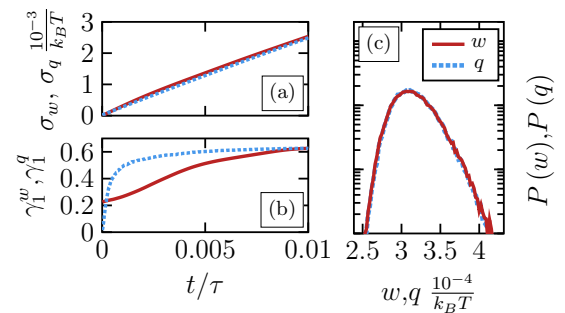

FIG. 5. (a) Standard deviation and (b) kurtosis of the heat (dashed, blue) and work distribution (solid, red) as a function of time for the disordered running (II) state $\dot{\gamma}\tau = 240$. (c) Corresponding distributions for integration times $t = 0.01\tau$.

The central limit theorem further predicts that the expected mean value is given by $E[w] = N E[w_i]$ and the standard deviation is $\sigma_N = \sqrt{N} \sigma_i$. Evaluating the heat distribution per particle $P(q_i)$ in equilibrium, we find that both relations hold and $P(q_i)$ is indeed close to that of the expected Bessel function, consistent with the predictions of the single-particle system.

At $\dot{\gamma} > 0$, the locked (I) state is characterized by elastic deformations of the (quadratic) equilibrium structure. This situation is reminiscent of that of a single particle in a harmonic potential $U(x, t) = k/2[x(t) - v\,t]^2$ which is now translated with constant velocity v through a resting solvent, inducing an effective solvent flow $u = -v$ [1,15,45]. We henceforth refer to this system as SP1. In SP1, the particle is pinned to the potential for all translation velocities v, which, due to the drag force, induces an elastic displacement of the particle from the trap center. In the steady state, both the work and heat are Gaussian-distributed, whose moments can be calculated analytically [45]. The mean work and heat $\langle w \rangle = \langle q \rangle \approx \mu^{-1} v^2 t$ are quadratic functions of the trap velocity v and increase linearly in time. The standard deviation of the distributions, e.g., for the work $\sigma_w \approx \sqrt{2 k_B T \langle w \rangle}$, is proportional to the square root of the mean. Comparing the flow velocities (u) from SP1 and the sheared colloidal film, we recognize that $v = -u \propto \dot{\gamma}$, which allows for a direct comparison. Inspecting our results for the sheared colloidal film, we find that $P(w)$ and $P(q)$ are indeed approximately Gaussian [see Fig. 2(d)] while the mean work $\langle w \rangle$ and heat $\langle q \rangle$ display a quadratic shear rate dependence [see Fig. 2(a)] and a linear increase in time (see Fig. 3). Further, the standard deviation of the work and heat is approximately given by $\sigma_{w/q} \approx \sqrt{2 k_B T \langle w \rangle}$, consistent with SP1, for all shear rates corresponding to the locked (I) state [see Fig. 4(a)]. Note that in our sheared film, σ_q displays a slight offset to larger values, whereas the standard deviation σ_w is slightly smaller than $\sqrt{2 k_B T \langle w \rangle}$ for small integration times. These differences become negligible for large integration times $t \to \infty$. Overall, we find that the results for w and q of the sheared colloidal film are in very good qualitative agreement with that of SP1.

Once the colloidal layers depin ($\dot{\gamma}\tau > 216$) the comparison to SP1 fails, as expected since the particles are displaced far from their original interstitials. In particular we observe that the work distribution becomes asymmetric for the disordered (II) running state [see Fig. 2(e)] and displays pronounced shoulders in the ordered running (III) state [see Fig. 2(f)]. We note that similar shoulders were observed for another system consisting of a single particle in a modulated double-well potential [46,47]. However, the origin of the shoulders in the sheared film is somewhat different. In fact, it is connected to a bistability of the ordered running (III) state, as discussed in the next section.

V. ORDERED RUNNING STATE

In Sec. V A, we first discuss in some detail the particle motion in the ordered running (III) state. Indeed, we have observed a new feature (not detected in our earlier studies), that is, a bistability. This feature has strong impact on the work and heat distributions, which we discuss in Sec. V B.
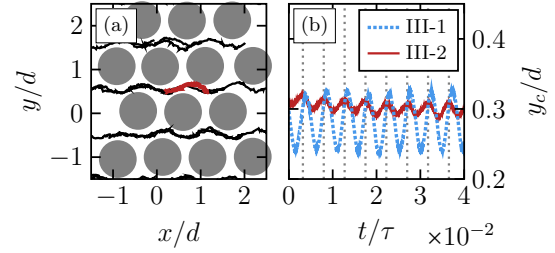

FIG. 6. (a) Segments of particle trajectories (black) of the top layer relative to the bottom layer (gray) at $\dot{\gamma}\tau = 400$. A full zigzag cycle of one particle is colored red for visibility. (b) Trajectories of the y component of the center of mass of one layer for two different systems. The gray dotted lines indicate the period of the zigzag motion, $\mathcal{T} = 0.00476\tau_B$.

A. Microscopic motion

The ordered running (III) state is characterized by a hexagonal in-plane order and collective, oscillatory *zigzag* motion of the particles of each layer. Specifically, the particle motion consists of periodic collective hopping from one interstitial of the neighboring layer to the next, as shown by the particle trajectories in Fig. 6(a). Note that one full zigzag cycle consists of two hopping events, where one is to the right ($y - \langle y \rangle < 0$) and the other to the left ($y - \langle y \rangle > 0$), with $\langle y \rangle$ being the average position.

The oscillatory motion is also reflected by the y component of the center-of-mass trajectories of the layers; see Fig. 6(b). As discussed in a previous study [32], the frequency of these center-of-mass oscillations ω_0 is related to the mean velocity $\langle \dot{x} \rangle$ and the periodicity in flow direction, x_0, of the hexagonal in-plane structure, according to $\omega_0 = 2\pi \dot{\gamma}_{\rm eff} \Delta z / x_0$. Here, $\dot{\gamma}_{\rm eff}$ is the effective shear rate extracted from the velocity profiles in the z direction $\dot{x}(z) \approx \dot{\gamma}_{\rm eff} z$; for details see Ref. [32]. The length scale x_0 remains approximately constant while $\langle \dot{x} \rangle$ increases linearly with the shear rate (see Fig. 1). As a result, the oscillation frequency is fully determined by the shear rate. Indeed, we find that the particle motion is synchronized with respect to their frequency for all shear rates corresponding to the ordered running (III) state.

However, a closer inspection of the center-of-mass trajectories of the individual realizations reveals that the amplitudes of the oscillations are not the same for all systems, in contrast to the frequency which remains constant. In fact, we find that the systems separate into two substates, which are characterized by either large (III-1) or small amplitudes (III-2) of the center-of-mass oscillations (see Fig. 13 in Appendix C). In other words, the running state is characterized by a bistability. Examples of the y component of the center-of-mass trajectories for both substates are plotted in Fig. 6(b) for $\dot{\gamma}\tau = 400$.

To understand the nature of the two substates we analyze the trajectories of individual particles of one layer. In particular, we calculate the Fourier transformation $\mathcal{F}_{y_i}(\omega_0)$ of the y trajectories of each particle i, where the frequency $\omega_0 = 2\pi/\mathcal{T}$ corresponds to the mean period $\mathcal{T}$ of the zigzag motion. We note that ω_0 corresponds to a maximum in the absolute value of the Fourier transform, as shown in Fig. 11 of Ref. [32]. Focusing now on the phase, i.e., $\Phi_i = {\rm Im}[\mathcal{F}_{y_i}(\omega_0)]$, we find that the spatial distribution of the phase is in general
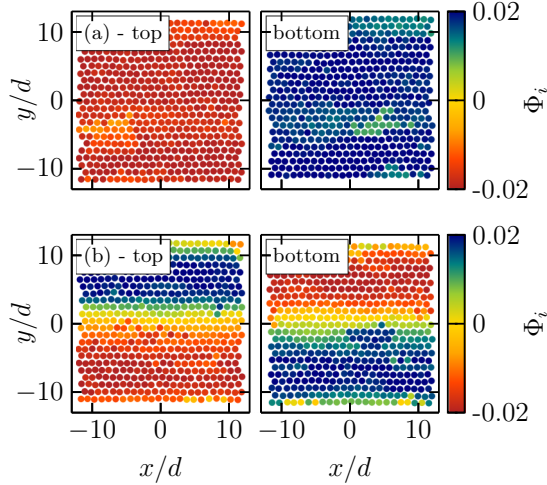
FIG. 7. Particle configurations inside the top (left) and bottom layer (right) for two different realizations corresponding to the in-phase (III-1) (a) and out-of-phase (III-2) substate (b) at shear rate $\dot\gamma\tau = 400$. The color indicates the phase of the dominant frequency of the particle trajectories.

inhomogeneous and differs significantly for both substates (III-1) and (III-2). This is visualized in Fig. 7.

For the first (III-1) substate, we find that Φ_i is approximately constant within the layer, as shown in Fig. 7(a) for the case $\dot\gamma\tau = 400$. This corresponds to the situation that the particle motion within the layer is fully synchronized with respect to their phase. Note that the y trajectories of the two layers are always in antiphase to each other. That is, when the particles of one layer jump to the left ($y - \langle y \rangle > 0$), the particles of the neighboring layer jump to the right ($y - \langle y \rangle < 0$), allowing for an efficient collective motion past each other in the presence of the slit-pore confinement. This synchronized motion then results in large amplitudes of the center-of-mass motion of the layers [see Fig. 6(b)].

For the second (III-2) substate, we find *two* domains with different phase Φ_i, as shown in Fig. 7(b) for a different realization at the same shear rate, $\dot\gamma\tau = 400$. That is, at the same time as some of the particles *within* the layer perform a jump to the left ($y - \langle y \rangle > 0$) others perform a jump to the right ($y - \langle y \rangle < 0$). As a result, the amplitudes of the center-of-mass oscillations are much smaller. In fact, for a perfect antiphase synchronized motion, of two domains of equal size, their oscillations would cancel each other perfectly, yielding a vanishing of the center-of-mass oscillations. According to our observations, however, the amplitude remains finite, reflecting that the particle motion is not fully synchronized in an antiphase manner. We understand that this stems from fluctuations of the domain size and the resulting extended interfacial regions. Inside these interfacial regions particle trajectories display a shift in phase such that they initiate hopping events at the same time as particles inside the two domains complete such events. As a result, the interface regions are out of sync with the two antiphase domains.

Given the observed bistability, it is an interesting questions to which extent this phenomenon depends on the size of the simulated system. Running test simulations we find that the two states indeed exist for a wide range of system sizes; see
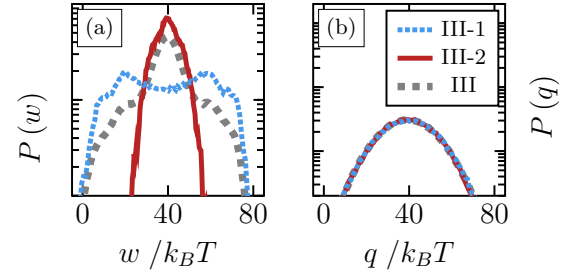

FIG. 8. (a) Work and (b) heat distribution for the in-phase (III-1, blue, dotted) and out-of-phase (III-2, red, solid) substate at shear rate $\dot\gamma\tau = 400$. The corresponding ensemble-averaged distributions (gray, dashed) are plotted for reference.

Appendix C for details. Only for very small systems containing $N < 338$ particles, the systems are always synchronized with respect to the phase. For larger systems ($338 < N < 3042$), we find that the probability to find either substate (III-1 or III-2) seems to be approximately independent of the system size [see Fig. 14(b) in Appendix C]. However, we expect that for very large systems ($N \to \infty$), the probability to find the fully synchronized state (III-1) should decrease significantly. We also note that the size of the domains is not constant for different system sizes. Also, there are rare cases where the system splits into four domains rather than in two. Overall we conclude that the bistability is not a result of the particular system size chosen in our simulations.

B. Work and heat distributions

With our findings concerning the bistability of the ordered running (III) state, we can now understand the ensemble-averaged work and heat in Fig. 2(f) as a superposition of the individual distributions corresponding to the substates III-1 and III-2. These distributions are plotted in Fig. 8. While $P(q)$ is the same, i.e., Gaussian, in both states [see Fig. 8(b)], $P(w)$ for the two states is very different, as shown in Fig. 8(a).

In particular for the first, fully synchronized substate (III-1), the work distribution displays a pronounced double-peaked structure, which can be related to the in-phase hopping of the particles. Specifically, the right-hand peak corresponds to the increased work required for particles to initiate a jump, whereas the left-hand peak corresponds to the decreased work required for particles to complete a jump. In fact, this situation is quite similar to that of a single particle driven on a periodic substrate (SP2), which we discuss in the next section.

For the second, partially synchronized substate (III-2), $P(w)$ displays a rather narrow single peak. We understand this as a result of the out-of-phase motion: Particles can initiate a jump at the same time as others complete one. In such a situation, the width of the work distribution is decreased such that the two individual peaks corresponding to an in-phase or antiphase motion cannot be resolved.

Overall, we find that the III-1 substate contributes to the shoulders observed in the ensemble-averaged work distributions $P(w)$ [see Fig. 2(f)], whereas the large central peak corresponds to the III-2 substate.

We note that *on average* the work and heat are the same in each of the substates. As discussed in Sec. IV A, this indicates
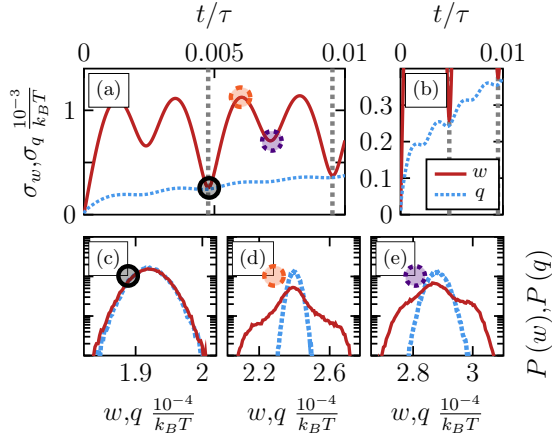
FIG. 9. (a) Standard deviation of the heat (dotted, blue) and work distribution (solid, red) as a function of time for the ordered running (III) substate $\dot{\gamma}\tau = 400$. The gray lines at $t = n0.00476\tau$ indicate the period of one full zigzag cycle of the colloidal layers, shown in Fig. 6(b). (b) Enlarged view of the standard deviation of the heat. (c)–(e) Corresponding distributions for three integration times $t = 0.00476, 0.006, 0.0072\tau$.

that both substates are indeed true steady states. It is then interesting to note that the mean work takes the same value for both substates. Furthermore, we have never observed a switching from one state to an other on the timescale of our simulations.

We now turn to the time dependence of the work and heat distribution in the ordered running (III) state (averaged over the two substates). Some results are shown in Figs. 9(a)–9(e).

In contrast to the locked (I) and the disordered running (II) state, $P(w)$ and $P(q)$ do *not* collapse onto a single distribution for the considered integration times. Instead, both evolve periodically in time, where the period $\mathcal{T} = 0.00476\tau$ agrees with that of the zigzag motion [see Fig. 6(b)]. The cyclic evolution, e.g., for $\dot{\gamma}\tau = 400$, is prominently reflected by the standard deviation $\sigma_{w/q}$ [see Figs. 9(a) and 9(b)] of the corresponding distributions, which in turn are shown in Figs. 9(c)–9(e) for three different integration times $t = 0.00476, 0.006, 0.0072\tau$. In particular, both $\sigma_{w/q}$ display two local minima in one cycle, where the first minimum at $t = n\mathcal{T}$ is deeper than the second at $t \approx (n + 0.5)\mathcal{T}$. Closer inspection reveals that $P(q)$ remains approximately Gaussian for all integration times, displaying only slight modulation of its width, as shown in the close-up in Fig. 9(b). In contrast, the shape of $P(w)$ changes markedly in one period. The periodic evolution of $P(w)$ can be understood as follows.

At the beginning of a new cycle, at integration times $t = n\mathcal{T}$, $P(w)$ conforms with $P(q)$, i.e., collapses onto a Gaussian distribution, as shown in Fig. 9(c) for $t = \mathcal{T}$. Here, all particles have performed on average *one* full zigzag cycle. For all realizations, the work consumed by this one cycle is approximately constant, leading to a narrow distribution of the integrated work. In fact, the collapse of $P(w)$ and $P(q)$ suggests that the work at these integration times is determined mostly by the thermal fluctuations of the bath.

Upon increasing the integration time, σ_w reaches another local minimum at $t = 0.0072\tau$ [see Fig. 9(a)]. Here, all particles have performed a full zigzag cycle as well as *one*

additional hopping of the next cycle. Again, due to the hopping events consuming an approximately constant amount of work, the width of $P(w)$ decreases. However, at this time, $P(w)$ and $P(q)$ do not collapse, as shown in Fig. 9(e). Instead, $P(w)$ displays pronounced asymmetric shoulders, stemming from the superposition of $P(w)$ of the individual substates (III-1) and (III-2). Similarly to the short-time distribution [see Fig. 8(a)], systems in the latter substate contribute to the central peak and systems in the former contribute to the shoulders. We note that this differs markedly from the distributions at integration times $t = n\mathcal{T}$ [see Fig. 9(c)], suggesting that the two hopping events corresponding to one full cycle are not identical.

At times $t = 0.006\tau$ and $t = 0.0082\tau$, both $\sigma_{w/q}$ display two local maxima [see Figs. 9(a) and 9(b)]. Here, the particles have performed, in addition to (at most) one jump of the current cycle, another segment of the full zigzag motion. These segments of the independent realizations are uncorrelated, leading to wide distributions of the heat and work. At these times, $P(w)$ displays rather wide symmetric shoulders [see Fig. 9(d)], stemming again from systems in the (III-1) substate.

VI. THERMODYNAMICS OF AN EFFECTIVE SINGLE-PARTICLE SYSTEM

To better interpret the cyclic evolution of $P(w)$ [see Fig. 9(a)], we consider in this section again a single-particle system. Indeed, to some extent, the hopping of the particles in the running state can be compared to the dynamics of a single particle driven on a periodic substrate potential [1,23,24]. In Ref. [34], we have developed a mapping strategy for the sheared colloidal film onto an effective one-dimensional model system, which estimates very well the location of the (depinning) transition from the locked (I) to the running (II and III) states of the sheared film. This (deterministic) model consists of a single particle subject to an effective sinusoidal potential $V(x) = V_0 \sin{(2\pi x/a_S)}$ driven by a constant flow u. In the absence of thermal noise, the equation of motion can be solved analytically. For small flow velocities u, the particle is unable to overcome the potential barriers of the sinusoidal potential, corresponding to the locked (I) state of the sheared film. Only for sufficiently large u, the particle is able to hop from one minimum to the next, corresponding to the ordered running (III) state. As shown in Ref. [34], the model (adapted to the quadratic substrate of our film) yields a depinning threshold in very good agreement with the numerical data. Moreover, it also captures key qualitative behavior for the running state.

To our knowledge, there are no analytical results for $P(w)$ and $P(q)$ in the case of a sinusoidal potential. We therefore present and discuss here numerical results for the stochastic thermodynamics of our effective model in the presence of thermal noise. The (overdamped) equation of motion reads

$$\dot{x} = \mu F_{\text{sub}}(x) + u + \dot{W}(t), \tag{14}$$

where μ is the mobility, F_{sub} is the force stemming from the substrate potential $V(x) = V_0 \sin{(2\pi x/a_S)}$, u is the constant solvent flow velocity, and δW is a random Gaussian displacement. Using the mapping strategy developed in [34],
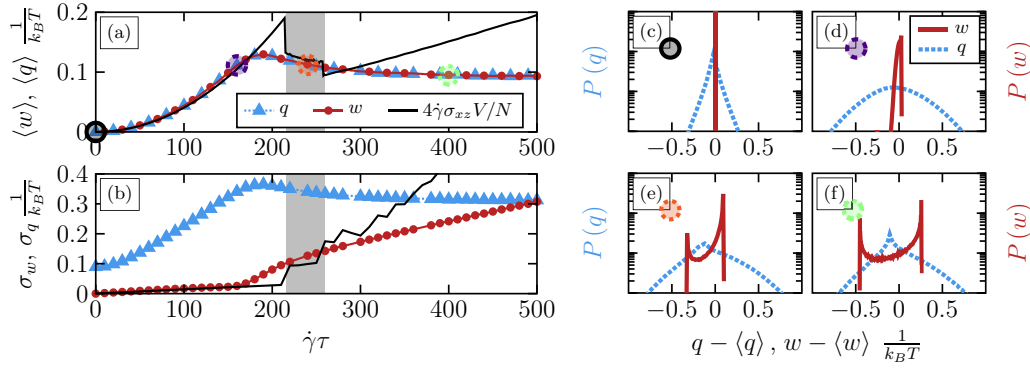
FIG. 10. (a) Mean value and (b) standard deviation of the work (red circles) and heat (blue triangles) integrated over short time intervals ($\Delta t = 10^{-5}\tau_B$); see Eq. (15) and Eq. (16), respectively. The mean is calculated by averaging over times τ_B and 100 *independent* systems. The black solid line stem from the estimation given in Eq. (10) for the full system rescaled by the number of particles N for the mean and $\sqrt{N}$ for the standard deviation, respectively. (c)–(f) Corresponding distributions of the work (solid, red) and heat (dashed, blue) for exemplary shear rates $\dot{\gamma}\tau = 0, 160, 240, 400$ (black, purple, orange, green circles), respectively.

we identify the flow $u = \dot{\gamma}\langle |z| \rangle$ of the single-particle system with the corresponding $\dot{\gamma}$ of the slit-pore system. The addition of thermal noise leads to thermally activated hopping events for shear rates below the depinning threshold $\dot{\gamma}\tau = 216$. This results in a continuous (rather than sharp) transition from the locked (I) to the running (III) state.

A. Work and heat distributions

For the effective single-particle system defined by Eq. (14), the expressions for the work and heat rates [see Eq. (4) and Eq. (5), respectively] simplify significantly, yielding

$$\dot{w}(t) = -u \sum_i F_{\text{sub}}(x), \tag{15}$$

$$\dot{q}(t) = \sum_i F_{\text{sub}}(x)[\dot{x}_i(t) - u]. \tag{16}$$

The corresponding work and heat are calculated by simple integration according to Eq. (6) and Eq. (7). We note that the expressions (15) and (16) are identical to that stemming from a particle subject to a sinusoidal potential that is translated with constant velocity u relative to the solvent, i.e., $V(x, t) = V_0 \sin[2\pi(x + ut)/a_S]$, where the work is given by $\dot{w} = \partial V(x, t)/\partial t$, yielding the same expression Eq. (15). The same holds for the heat rate.

Focusing first on the shear dependency of the mean work $\langle w \rangle$ and heat $\langle q \rangle$ for short integration times $t = 10^{-5}\tau$, plotted in Fig. 10(a), we find that $\langle w \rangle = \langle q \rangle$ are equal for all shear rates. Starting from the equilibrium ($\dot{\gamma} = 0$), where both the mean work and heat vanish, and applying a constant flow u, $\langle w \rangle$ displays a pronounced quadratic increase for shear rates corresponding to the locked (I) state. As discussed in Sec. IV C, the quadratic shear rate dependence stems from the elastic displacement of the particle from the (approximately harmonic) minimum of the substrate potential. Once the particle depins from the substrate, the work and heat decrease and saturate for large shear rates corresponding to the running (III) state. That is, for large shear rates, the impact of the substrate potential becomes negligible and driving the system by a constant flow requires on average a constant supply of work.

Turning now to the distribution functions, we find that at $\dot{\gamma} = 0$, $P(w)$ and $P(q)$ agree with those for model SP1 (see Sec. IV C). Applying the flow field $u = \dot{\gamma}\langle |z| \rangle$, $P(q)$ becomes Gaussian whereas $P(w)$ displays a slight negative skewness ($\gamma_1^w > -0.5$), as shown in Fig. 10(d). Once the particle depins, $P(w)$ transitions to a pronounced bimodal distribution displaying two sharp peaks [see Figs. 10(e)–10(f)], which correspond to the initiation and completion of a hopping event. Here, the sharp bounding of $P(w)$ can be understood from the equation of the work rate Eq. (15), which for a constant flow velocity u is bounded by $\pm F_{\text{max}} = V_0 2\pi/a_S$. Note that the right peak, corresponding to the particle initiating a jump, is much higher than the left, which corresponds to the relaxation towards the next minimum. This stems from the fact that the buildup phase initiating a jump is much slower than the subsequent relaxation. As a result, for large shear rates, the height difference between the left and right peak decreases, due to the jumping becoming more regular [see Figs. 10(e)–10(f)]. Finally, in this state, the heat distribution $P(q)$ becomes non-Gaussian again, displaying two asymmetric flanks as well as a sharp peak near the middle.

The work $P(w)$ and heat distributions $P(q)$ depend not only on the shear rate but also on the integration time t. Here, we focus on the integration time dependence of $P(w)$ and $P(q)$ in the running state, which both display a cyclic time evolution [with that of $P(w)$ being more pronounced than that of $P(q)$], as shown in Fig. 11. This cyclic evolution is characterized by local minima in the standard deviation of
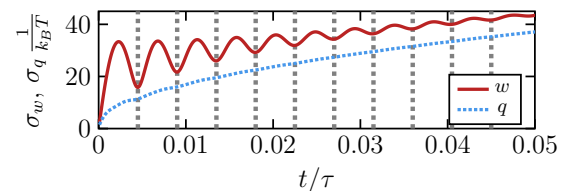

FIG. 11. Standard deviation of the heat (dashed, blue) and work distribution (solid, red) as a function of time for the running state $\dot{\gamma}\tau = 400$ of the single-particle system. The period of one hopping cycle $T = 0.0045$ is indicated by dashed gray lines.

$P(w)$ and $P(q)$ at integration times $t = n\mathcal{T}$, corresponding to multiples of the mean period $\mathcal{T} = 0.0045$ one particle takes to jump from one minimum to another. At these times, all particles have performed one jump on average, which approximately consumes a fixed amount of work. As a result, $P(w)$ is mostly determined by the thermal fluctuations, thus leading to distributions similar to $P(q)$. In between these minima, the integration includes, in addition to a multiple of full jumps, an additional segment of the next jump. Due to the independent choice of initial states, these segments are mostly uncorrelated, resulting in wide distributions of the work. This cyclic evolution displays a pronounced damping, which reflect the fact that the oscillating particle motion becomes increasingly uncorrelated over time. We attribute this to the thermal fluctuation driving the diffusion of the particles.

B. Comparison to the sheared film

Comparing the effective single-particle system to the sheared colloidal film, we find many similarities. As expected, we find quantitative agreement of the mean work and heat for shear rates corresponding to the locked state, as can be already understood via SP1 (see Sec. IV C).

Here, we focus on the running state. Comparing Figs. 10(e)–10(f) and Fig. 8, we realize that the work distribution $P(w)$ of the single-particle system indeed resembles that of the in-phase (III-1) running state of the sheared film: The latter also displays two peaks corresponding to the initiation and completion of a jump. The key difference is that for the single-particle system, the two peaks are very sharp due to the boundedness of the substrate potential ($\pm F_{\max} = V_0 2\pi/a_S$), whereas the sheared film displays much wider peaks. This stems from the fact that in the slit pore, the "substrate" is a layer of particles which itself is subject to fluctuations. As a result, the force required to initiate a jump is not constant, but a stochastic quantity itself, leading to wider peaks in $P(w)$.

Another similarity is that $P(w)$ evolves in a cyclic manner, where the period is determined by the average time $\mathcal{T}$ a particle needs to finish a jumping cycle. For the single-particle system, where each jump is identical, the time evolution is modulated by simple decaying oscillations. In contrast, in the sheared film, each cycle displays two local minima as well as two maxima in between. This more complex evolution stems from the fact that in the sheared film the particles need to perform two jumps in order to complete a cycle.

VII. CONCLUSIONS

Using Brownian dynamics simulation we have investigated the stochastic thermodynamics of a thin colloidal film under planar shear flow. Focusing on a particular parameter set corresponding to high density and strong spatial confinement, the colloids arrange, already in equilibrium, in two crystalline layers with quadratic in-plane order. Applying the linear shear flow, the system displays three distinct steady states [32,34,35]. Using the framework of stochastic thermodynamics, we have calculated the work and heat of this many-particle system for all steady states, employing the expressions suggested in Ref. [36]. We find that, *on average*, both the work

and heat are related to the shear stress component of the configurational stress tensor, which is a common feature of shear-driven systems [25,29,44]. Consistent with the shear stress, we therefore find jumps in the mean work and heat as a function of the shear rate, marking the borders of the domains of the steady states. That is, all transitions between the three steady states are clearly reflected already in the *mean* work and heat. Moreover, the transitions are also reflected by the change of the shape of the work and heat distributions, respectively, and their time evolution. We expect this to be a general result for (flow-)driven many-particle systems. Of course, the details of the distributions should depend on relevant system parameters, as do the observed steady states. For example, a sheared film with three layers (i.e., larger L_z) displays an intermediate state [33], and we would expect corresponding changes in the distributions.

For the present system, particularly interesting distributions are found in the ordered running state, where the *ensemble-averaged* work distribution reflects a bistability regarding the degree of phase synchronization of the particle motion. Here, one substate is characterized by global in-phase particle motions, whereas the other substate consists of two domains with opposite phase as well as extended interfacial regions. The ensemble-averaged work distribution is then a superposition of these substates, with a pronounced central peak and asymmetric shoulders. This is a nice example of how fluctuations of thermodynamic quantities indicate an underlying complex many-particle behavior.

To some extent, we can understand the work and heat distributions of the sheared colloidal film by comparing to appropriate single-particle systems. For the locked state, we find that the corresponding shear rate and time dependence of the work and heat distributions is in good agreement with that of a single particle trapped in a harmonic trap which is translated with constant velocity [45]. For the ordered running state, in particular the in-phase substate, we can understand the work distributions by comparing to a single particle on a sinusoidal periodic potential driven by a constant flow. In both cases, the work distributions display two peaks corresponding to the initiation and completion of hopping events, which evolve cyclically in time. Overall, states where the individual particle motion is fully coherent are well described by effective single-particle models for the center of mass. The many-body character of the sheared film becomes apparent when the particle motion is disordered or only partially synchronized, as observed for the disordered running state and the out-of-phase substate.

One open question is the role of entropy production and related fluctuation theorems [1,26] for many-particle systems under shear. In general, the entropy production is defined via the path probabilities of the particle trajectories [48]. However, a derivation of these path probabilities for dense many-particle systems driven out of equilibrium is not trivial. Therefore, one major challenge is to find appropriate expressions or methods to accurately compute the instantaneous entropy production from particle-based simulations or experiments for shear-driven systems (and related systems such as colloidal nanoclutches [49]). One strategy might be to consider the limit of long integration times and small system sizes, where the distributions of the total entropy production and the heat

collapse [1]. In this limit, one should recover steady state fluctuation theorems for the heat distributions, as was done in Ref. [25]. Work in this direction is in progress.

APPENDIX A: STRATONOVICH CALCULUS

It is well known that when calculating the derivatives and integrals of stochastic quantities, extra care has to be taken [50] due to the fact that the rules of stochastic calculus are ambiguous. In our numerical calculations we employ the Stratonovich calculus, consistent with the fact that this calculus was used to *derive* the equations for the work and heat rates [see Eqs. (4) and (5)]. To this end, the stochastic velocity $\dot{\mathbf{r}}_i(t)$ is determined using the midpoint rule

$$\dot{\mathbf{r}}_i(t) \approx \frac{\mathbf{r}_i(t + \Delta t) - \mathbf{r}_i(t - \Delta t)}{2\Delta t}, \tag{A1}$$

where $\Delta t = 10^{-5}\tau_B$ is the time step of our BD simulations. We note that using this definition is key to calculate the work and heat rates given in Eqs. (8) and (9). In particular, the Stratonovich rule ensures that the correlation terms, such as $\langle \mathbf{F}_i(t) \cdot \mathbf{r}_i(t \pm \Delta t) \rangle$ arising in Eq. (9), cancel properly. Indeed, not using the midpoint rule may lead to unphysical results, such as a finite mean heat rate ($\langle \dot{q} \rangle > 0$) already in equilibrium.

Further, in order to calculate the work and heat we need to integrate the work $\dot{w}_i(t)$ and heat rate trajectories $\dot{q}_i(t)$ numerically [see Eqs. (6) and (7)]. The corresponding integrals in the framework of the Stratonovich calculus, e.g., for the work, are given by

$$w_i(t) = \int_{t_1=0}^{t_N=t} \dot{w}_i(s)ds \approx \sum_{j=1}^{N-1} \frac{\dot{w}_i(t_{j+1}) + \dot{w}_i(t_j)}{2}\Delta t, \tag{A2}$$

where $t_{j+1} = t_j + \Delta t$ is a discrete series of times with N entries and the step size $\Delta t = 10^{-5}\tau_B$. The integral for the heat is evaluated in the same manner.

APPENDIX B: EXTERNAL FORCE INTERPRETATION

In previous studies [34], we have shown that one can understand the transition from the locked (I) to the running (II and III) states in the sheared film as a depinning transition. Therefore, our systems shares many similarities to driven monolayer systems, which consist of a single crystalline layer of colloids driven by constant force over an periodic substrate potential. In a recent experimental study [28], the stochastic thermodynamics of the latter system was investigated, reporting the work distributions for the pinned and running steady state. The study finds that in the pinned state the mean work done on the system vanishes, contrary to our findings according to which work is required to maintain the elastic deformations of the colloidal crystal layers. In fact, this discrepancy is a result of an alternative interpretation of
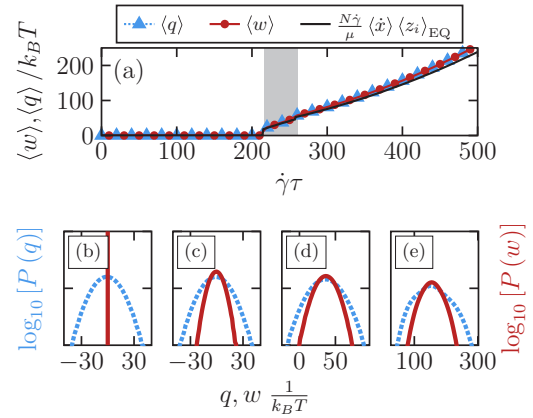

FIG. 12. (a) Mean short-time ($t = 10^{-5}\tau_B$) work (solid, red) and heat (dashed, blue) averaged over τ_B and 100 systems for the flow [see Eq. (B1) and Eq. (B2)]. The black dashed and solid lines stem from the estimation given in Eq. (B3). (b)–(e) Corresponding distributions of the work (solid, red) and heat (dashed, blue) for exemplary shear rates $\dot{\gamma}\tau = 0, 160, 240, 400$, respectively.

the driving mechanism, where one assumes an external force $f_i = \mu^{-1}\mathbf{u}(\mathbf{r}_i)$ proportional to the flow field.

Applying this interpretation to our slit-pore system, i.e., setting $\mathbf{u}_i = 0$ and $\mathbf{f}_i = \mu^{-1}\dot{\gamma}z_i\mathbf{e}_x$, the expressions for the work Eq. (4) and heat rates Eq. (5) reduce to

$$\dot{w}(t) = \sum_i \mathbf{f}_i \cdot \dot{\mathbf{r}}_i(t), \tag{B1}$$

$$\dot{q}(t) = \sum_i [\mathbf{f}_i + \mathbf{F}_i(\{\mathbf{r}\}, t)] \cdot \dot{\mathbf{r}}_i(t). \tag{B2}$$

Explicitly inserting the linear shear force $\mathbf{f}_i = \mu^{-1}\dot{\gamma}z_i\mathbf{e}_x$ into Eq. (B1) yields further simplifications

$$\dot{w}(t) = \frac{\dot{\gamma}}{\mu} \sum_i z_i \dot{x}_i(t) \approx \frac{\dot{\gamma}}{\mu} \sum_i \langle z_i \rangle_{\text{EQ}} \dot{x}_i, \tag{B3}$$

where $\langle z_i \rangle_{\text{EQ}}$ is the mean position of particle i in equilibrium. In the last part of Eq. (B3), we used that due to the strong confinement, which restricts the z position of the layers, the position of the individual particles is approximately constant such that $z_i \approx \langle z_i \rangle_{\text{EQ}}$. Equation (B3) therefore shows that the work rate is approximately proportional to the velocity of the particles. The corresponding work and heat are again obtained by integrating according to Eqs. (6) and (7).In Fig. 12(a), we have plotted the mean work $\langle w \rangle$ and heat $\langle q \rangle$ for short integration times $t = 10^{-5}\tau_B$ using Eqs. (B1) and (B2). Focusing on the work, starting in equilibrium, we find that $\langle w \rangle$ again vanishes, as expected in the absence of any driving forces. However, applying a shear force, $\langle w \rangle$ remains zero for the locked steady state ($\dot{\gamma}\tau < 216$) and jumps to nonzero values only for shear rates corresponding to the unordered running state ($\dot{\gamma}\tau > 216$). For large shear rates ($\dot{\gamma}\tau > 260$), corresponding to the ordered running state, $\langle w \rangle$ displays a quadratic increase. Again, we find that the domains of the different steady states are clearly reflected already in the mean work and heat, which are equal for all considered shear rates.

Examining now the distribution of the work $P(w)$ [see Figs. 12(b)–12(e)], we find that $P(w)$ is delta-peaked in
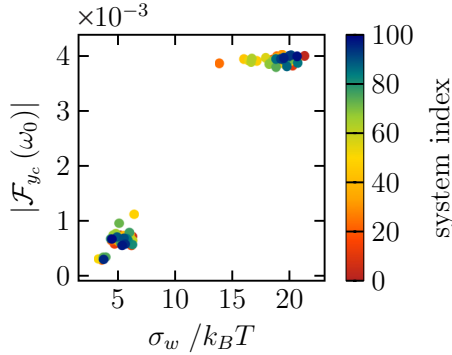
FIG. 13. Scatter plot of 100 realizations in the ordered running state (III) at shear rate $\dot{\gamma}\tau = 400$. The x axis denotes the standard deviation of the short-time work distributions [see, e.g., Fig. 8(a)], whereas the y axis denotes the amplitude of the dominating frequency ω_0 of the oscillating center-of-mass trajectories y_c [see, e.g., Fig. 6(b)], which are given by the respective absolute value of the Fourier transformation. The color denotes the arbitrary index of the system.
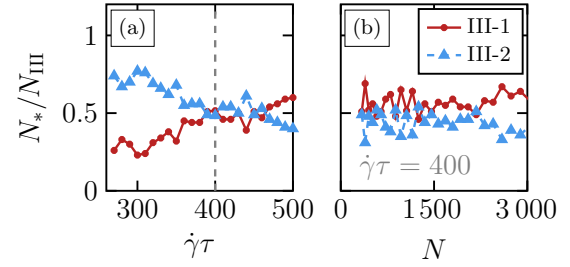

FIG. 14. (a) Percentage of systems in substate III-1 (red circle) and III-2 (blue triangle) as a function of the shear rate at fixed system size $N = 1058$. (b) Percentage of systems in substate III-1 (red circle) and III-2 (blue triangle) as a function of the system size N at fixed shear rate $\dot{\gamma}\tau = 400$. The total number of individual realizations N_{III} is 100 for all simulations.

equilibrium and approximately Gaussian for all other steady states. Only for longer integration times, $P(w)$ displays asymmetric shoulders. These results are consistent with the findings from Ref. [28]. In our simulations we can further calculate the heat distributions, which are again Gaussian for the locked (I) and unordered running (II) state; see Figs. 2(b)–2(d). Interestingly, in the ordered running (III) state ($\dot{\gamma}\tau > 260$), the heat distribution displays pronounced asymmetric shoulders.

The discrepancy between the results in the flow (see Sec. IV) and the force interpretation discussed in this section originates from the choice of frame of reference. For the driven monolayer in its locked state, the particles are unable to follow the flow. In the frame of reference of the solvent, the particles move on average with the flow velocity, requiring a continuous supply of work and corresponding to the flow interpretation. In contrast, in the frame of reference of the substrate the particles are elastically displaced from their respective potential minima by a force proportional to the flow velocity, leaving the particles motionless on average. This does not require any work and corresponds to the force interpretation. Here, the work done by the flow on the particles is excluded from the system of interest and instead included in the energy of the bath, i.e., the heat.

APPENDIX C: ORDERED RUNNING SUBSTATE STATISTICS

In Sec. V, we have discussed the bistability of the running (III) state with respect to the phase synchronicity of the particle motions. We find that in a single realization, the system is either fully (III-1) or partially (III-2) synchronized, corresponding to the two substates. These two states are clearly reflected in Fig. 13, where 100 realizations of the running state at $\dot{\gamma}\tau = 400$ are plotted with respect to the standard deviation σ_w of the corresponding short-time work distributions [see, e.g., Fig. 8(a)] on the one hand and the amplitude of the dominating frequency of the center-of-mass trajectories y_c [see, e.g., Fig. 6(b)] on the other hand. The amplitude is given by the absolute value of the corresponding Fourier transformation $|\mathcal{F}_{y_c}(\omega_0)|$. We find that all realizations contribute to one of two clusters, representing the two substates. Here, the in-phase (III-1) substate corresponds to the cluster with large standard deviation of the work distribution and amplitudes of the center-of-mass trajectories, i.e., upper right, whereas the out-of-phase (III-2) substate corresponds to the cluster at small standard deviations and amplitudes, i.e., lower left.

In Fig. 14 we compare the number of systems corresponding to the substates III-1 and III-2, respectively. We find that the partially synchronized (III-2) substate is more likely for small shear rates and the number of systems in this state decreases continuously with increasing shear rate, as shown in Fig. 14(a). In other words, the fully synchronized (III-1) state becomes more likely with increasing shear rate.

Varying now the system size N, i.e., the number of particles, for a fixed shear rate $\dot{\gamma}\tau = 400$, we find that the number of systems in either substate remains approximately constant; see Fig. 14(b). Indeed, only for very small systems ($N < 338$) the particle motion is always fully synchronized and domains with different phases were not observed. Going to larger systems ($N > 338$), we observe both substates for all considered N.

[1] U. Seifert, Rep. Prog. Phys. **75**, 126001 (2012).

[2] K. Sekimoto, *Stochastic Energetics*, edited by C. Caron, Lecture Notes in Physics (Springer, 2010), Vol. 799.

[3] C. Van den Broeck and M. Esposito, Phys. A **418**, 6 (2015).

[4] S. Ciliberto, Phys. Rev. X **7**, 021051 (2017).

[5] R. Astumian, Science **276**, 917 (1997).

[6] J. A. Wagoner and K. A. Dill, J. Phys. Chem. B **120**, 6327 (2016).

[7] U. Seifert, Eur. Phys. J. E **34**, 26 (2011).
[8] S. Ciliberto, A. Imparato, A. Naert, and M. Tanase, Phys. Rev. Lett. **110**, 180601 (2013).
[9] T. Speck, Europhys. Lett. **114**, 30006 (2016).
[10] D. Mandal, K. Klymko, and M. R. DeWeese, Phys. Rev. Lett. **119**, 258001 (2017).
[11] F. S. Gnesotto, F. Mura, J. Gladrow, and C. P. Broedersz, Rep. Prog. Phys. **81**, 066601 (2018).
[12] M. Campisi, P. Haenggi, and P. Talkner, Rev. Mod. Phys. **83**, 771 (2011).
[13] P. Strasberg, G. Schaller, T. Brandes, and M. Esposito, Phys. Rev. Lett. **110**, 040601 (2013).
[14] C. Elouard, N. K. Bernardes, A. R. R. Carvalho, M. F. Santos, and A. Auffeves, New J. Phys. **19**, 103011 (2017).
[15] G. M. Wang, E. M. Sevick, E. Mittag, D. J. Searles, and D. J. Evans, Phys. Rev. Lett. **89**, 050601 (2002).
[16] C. Maggi, M. Paoluzzi, N. Pellicciotta, A. Lepore, L. Angelani, and R. Di Leonardo, Phys. Rev. Lett. **113**, 238303 (2014).
[17] M. L. Rosinberg, G. Tarjus, and T. Munakata, Phys. Rev. E **95**, 022123 (2017).
[18] E. Trepagnier, C. Jarzynski, F. Ritort, G. Crooks, C. Bustamante, and J. Liphardt, Proc. Natl. Acad. Sci. U.S.A. **101**, 15038 (2004).
[19] G. E. Crooks, Phys. Rev. E **60**, 2721 (1999).
[20] I. Cohen, T. G. Mason, and D. A. Weitz, Phys. Rev. Lett. **93**, 046001 (2004).
[21] J. Gieseler, L. Novotny, C. Moritz, and C. Dellago, New J. Phys. **17**, 045011 (2015).
[22] I. A. Martinez, E. Roldan, L. Dinis, and R. A. Rica, Soft Matter **13**, 22 (2017).
[23] A. Gomez-Marin and I. Pagonabarraga, Phys. Rev. E **74**, 061113 (2006).
[24] X.-g. Ma, Y. Su, P.-Y. Lai, and P. Tong, Phys. Rev. E **96**, 012601 (2017).
[25] D. J. Evans, E. G. D. Cohen, and G. P. Morriss, Phys. Rev. Lett. **71**, 2401 (1993).
[26] J. Ehrich and A. Engel, Phys. Rev. E **96**, 042129 (2017).
[27] A. Imparato, New J. Phys. **17**, 125004 (2015).
[28] J. R. Gomez-Solano, C. July, J. Mehl, and C. Bechinger, New J. Phys. **17**, 045026 (2015).

[29] S. H. E. Rahbari, A. A. Saberi, H. Park, and J. Vollmer, Nat. Commun. **8**, 11 (2017).
[30] A. K. Balin, A. Zottl, J. M. Yeomans, and T. N. Shendruk, Phys. Rev. Fluids **2**, 113102 (2017).
[31] D. Derks, Y. L. Wu, A. van Blaaderen, and A. Imhof, Soft Matter **5**, 1060 (2009).
[32] T. A. Vezirov and S. H. L. Klapp, Phys. Rev. E **88**, 052307 (2013).
[33] S. Gerloff, T. A. Vezirov, and S. H. L. Klapp, Phys. Rev. E **95**, 062605 (2017).
[34] S. Gerloff and S. H. L. Klapp, Phys. Rev. E **94**, 062605 (2016).
[35] T. A. Vezirov, S. Gerloff, and S. H. L. Klapp, Soft Matter **11**, 406 (2015).
[36] T. Speck, J. Mehl, and U. Seifert, Phys. Rev. Lett. **100**, 178302 (2008).
[37] S. H. L. Klapp, D. Qu, and R. v. Klitzing, J. Phys. Chem. B **111**, 1296 (2007).
[38] J.-P. Hansen, *Theory of Simple Liquids: With Applications to Soft Matter* (Elsevier, Amsterdam, 2013).
[39] R. Messina and H. Lowen, Phys. Rev. E **73**, 011405 (2006).
[40] T. H. Besseling, M. Hermes, A. Fortini, M. Dijkstra, A. Imhof, and A. van Blaaderen, Soft Matter **8**, 6931 (2012).
[41] J. Delhommelle, J. Petravic, and D. Evans, J. Chem. Phys. **119**, 11005 (2003).
[42] J. J. Cerdà, T. Sintes, C. Holm, C. M. Sorensen, and A. Chakrabarti, Phys. Rev. E **78**, 031403 (2008).
[43] B. Lander, U. Seifert, and T. Speck, J. Chem. Phys. **138**, 224907 (2013).
[44] T. Speck, arXiv:1707.05289.
[45] A. Imparato, L. Peliti, G. Pesce, G. Rusciano, and A. Sasso, Phys. Rev. E **76**, 050101(R) (2007).
[46] A. Imparato, P. Jop, A. Petrosyan, and S. Ciliberto, J. Stat. Mech. (2008) P10017.
[47] H. C. Fogedby and A. Imparato, J. Phys. A **42**, 475004 (2009).
[48] U. Seifert, Phys. Rev. Lett. **95**, 040602 (2005).
[49] A. Ortiz-Ambriz, S. Gerloff, S. H. L. Klapp, J. Ortin, and P. Tierno, Soft Matter **14**, 5121 (2018).
[50] N. van Kampen, J. Stat. Phys. **24**, 175 (1981).